Analysis of the stress distribution in a laminar direct simple shear device and implications for test data interpretation

Michelle L. Bernhardt-Barry[a], Giovanna Biscontin[b], and Catherine O'Sullivan[c]

[a]Associate Professor, Department of Civil Engineering, University of Arkansas, Arkansas, USA, email: mlbernha@uark.edu, phone: (479)575-6027
[b]Lecturer, Department of Engineering, Cambridge University, Cambridge, UK
[c]Professor, Department of Civil and Environmental Engineering, Imperial College London, London, UK

ABSTRACT

Direct simple shear (DSS) testing allows observation of load-deformation response under rotation of the major principal stress plane, which is descriptive of many actual field problems. While the simplicity of the test configuration makes its use popular in research and industry, key uncertainties still remain regarding the interpretation of the laboratory data. This study uses laboratory validated discrete element method (DEM) models to examine the stress transmission in laminar-type direct simple shear devices under drained constant effective stress conditions. The DEM models (comprised of spheres) closely replicate physical specimens of precision chrome steel ball bearings for which the properties (e.g., shape, surface friction, and stiffness) were measured directly. The DEM models were also validated using experimental tests, so that conclusions regarding the system response can be derived with confidence from the available DEM data. The testing program included both loose and dense specimens, allowing for a comparison of the influence of density on stress state which has not been examined in previous simple shear DEM studies. Differences were observed between vertical effective stresses and shear stresses derived from boundary measurements (as commonly carried out in experimental programs) and those derived from force measurements within the DEM specimens. The failure state of the material in simple shear was also examined through Mohr's circles of stress. The evolution of stresses on both the horizontally and vertically oriented planes were considered so that established methods of direct simple shear interpretation could be critically assessed. For the loose specimens, the angle of shearing resistance can be confidently estimated considering the maximum shear stress acting on the horizontal plane, which is easily inferred from measurements of the shear force during the physical test. This was true considering both internal and boundary calculated stresses. This approach, however, is inaccurate for the dense specimens. Analysis of the particle-scale kinematics of the response illustrates that the deformation field within the central portion of the specimen is in simple shear, although the magnitude of this shearing was significantly larger than what was measured on the boundary. This study and the conclusions derived focus on smooth spherical particle specimens; the objective was to examine the stress distribution within DSS devices and the implications for test interpretation using DEM models that more closely matched the physical laboratory specimens tested than in previous studies. When considered alongside the existing studies, the findings show that there is no broad conclusion that can be applied for all materials and all conditions in simple shear and that interpretation should be carefully tied to the physical conditions simulated.

KEYWORDS: Discrete element method (DEM), laboratory testing, granular materials

INTRODUCTION

Researchers have shown that the in-situ stress state and mode of soil deformation for a number of practical geotechnical problems can be best replicated by simple shear testing (e.g., [5, 6, 243, 29]). While a number of research studies have highlighted limitations of the direct simple shear (DSS) apparatus [2, 23, 36, 40], the simplicity of the test setup and the smooth rotation of the principal stress planes have contributed to its popularity. One of the main limitations of DSS testing is that interpretation of strength parameters is non-trivial because of the inability to measure the normal forces on the vertically oriented specimen boundaries. To overcome this, a number of possible failure assumptions has been developed, each of which invokes hypotheses regarding the actual stress state within the soil element. Past researchers have examined this experimentally and numerically using continuum methods (e.g., [7, 8, 9, 39, 45, 46]), but more recently the potential to use discrete element method (DEM) simulations to analyze the DSS test has been demonstrated in the literature (e.g. [3, 16, 44]). While previous DSS experimentalists devised innovative ways to measure local forces around a specimen, their systems were limited to a few boundary point measurements, and any internal stress state had to be inferred from these measurements. DEM models provide a means of calculating the internal and boundary stresses. Out of the handful of DEM studies in the literature, all have limited their analyses to a single packing density and only considered internal stresses and there is still little understanding of how the data gained in an experimental test should be properly analyzed.

This research extends earlier DEM studies of the DSS test by comparing internal stress states and boundary-derived stresses for specimens of an ideal granular material (i.e., spheres) with two different initial densities in a stacked-ring NGI-type DSS device under drained constant effective stress conditions. The DEM models have been carefully validated using equivalent laboratory tests with precision spherical chrome steel ball bearings [4] to ensure that any conclusions made are robust and not due to modeling assumptions or simplifications. After a brief discussion of the background, the paper describes the DEM simulation approach adopted including representative data from the experimental validation. The internal stress transmission data in the DEM specimens are then used to analyze the effects of specimen density on stress inhomogeneities, and the existing approaches for determining the angle of shearing resistance from DSS tests are analyzed. A comparison of the stress state determined from internal measurements and from boundary measurements is also made to further examine the existing approaches for analyzing experimental results. Particle displacements are then analyzed to examine the deformation field within the specimens and any relationship to the stress state.

BACKGROUND

The DSS apparatus is available in two forms: a cylindrical specimen enclosed by either a wire-reinforced membrane or stack of rings, and a parallelepiped specimen bounded by rigid walls. The cylindrical DSS device was originally developed in 1936 at the Swedish Geotechnical Institute [25] and is now typically referred to as the NGI-type DSS because of modifications made at the Norwegian Geotechnical Institute [5]. The parallelepiped specimen form is termed the Cambridge-type DSS due to developments made at Cambridge University by Roscoe [34]. The DSS apparatus aims to replicate plane strain simple shear conditions by applying an approximately uniform shear strain field to the specimen and allowing the principal stress and strain axes to rotate smoothly, a feature which is not possible in triaxial testing. Because of the commercial availability, the ease of specimen preparation, and the fact that natural samples are generally retrieved using cylindrical samplers, the NGI-type device has become more common in practice and in research, and thus, is the focus of this paper.

Although the test aims to create a conceptually simple strain field, implementation of the ideal conditions has been difficult to attain. Only the normal and shear loads on the top or bottom boundary (i.e., horizontally oriented boundaries) are typically measured in routine DSS tests and no information is available for the radial face (i.e., vertically oriented boundary) of the specimen. Fig. 1 illustrates the boundary terminology and loading schemes for typical DSS tests, as used in this study. Without measurements of the stresses on the vertically oriented boundary, the complete stress state within the specimen cannot be defined. Also, neither the NGI nor the Cambridge device is capable of applying complementary shear stresses on the lateral face (i.e. radial face for the NGI device) of the specimen, which leads to non-uniform distributions of the normal and shear stresses across the top and bottom horizontally oriented boundaries. According to Shen et al. [38] and Franke et al. [20], the area over which these non-uniformities exist can be minimized if the diameter to height ratio is large (>3.75).

While non-uniformities exist, most studies show that the core region of the specimen is under uniform stress and strain conditions [10, 18, 19, 28, 33, 34, 38]. Through elaborate instrumentation on both the Cambridge and the NGI-type devices, Budhu [7] showed that the specimen core (measured using a central load cell on the horizontal boundary) was relatively unaffected by non-uniformities and that reliable normal and shear stress information could be obtained from this region of the specimen. Wood et al. [45] and Budhu [8] also showed that the complete stress state could be defined for the highly instrumented Cambridge-type DSS, however, even when the radial boundary was instrumented on the NGI-type DSS device, Budhu [8] found that the stresses were not equal to the intermediate principal stresses or the horizontal normal stresses.

Because the stresses on the vertically oriented boundary are not known in the NGI-type device, assumptions must be made in order to identify the orientation and magnitude of the principal stresses and ultimately the strength parameters of the soil. A number of approaches and corresponding assumptions have been developed through the years; however, there is still some discussion as to which is most appropriate for DSS analyses. The most conventional failure assumption says that the horizontally oriented planes are the planes of maximum stress obliquity (referred to as Assumption 1 here). The orientation of the major principal stress with the horizontal is then $45° + \phi'/2$, and the angle of shearing resistance (ϕ') is the inverse tangent of the stress ratio, i.e., $\phi' = tan^{-1}(\tau_{xz}/\sigma'_{zz})$, where the shear stress τ_{xz} and the normal stress σ'_{zz} are calculated based on measurements taken on the horizontally oriented specimen boundary. This is the general assumption for the direct shear test; however, for drained constant stress simple shear tests, Roscoe et al. [35] and Airey et al. [2] showed that the failure plane was not horizontal. A second approach assumes that the horizontally oriented planes are planes of maximum shear stress (Assumption 2). The major principal stress is thus oriented at 45° from the horizontal and the angle of shearing resistance is the inverse sine of the stress ratio, i.e. $\phi' = sin^{-1}(\tau_{xz}/\sigma'_{zz})$. An additional failure condition suggested by de Josselin de Jong [17] proposed the possibility of failure occurring on either horizontally oriented planes or a combination of sliding and rotation on vertically oriented planes (Assumption 3). If the vertically oriented planes are assumed to be the failure plane, the major principal stress plane is then oriented at $45° - \phi'/2$ with respect to the horizontal, and the angle of shearing resistance is the inverse tangent of the ratio of the shear stress to the normal stress on the vertically oriented plane. Budhu [9] suggested that for drained tests on sand, the failure is initiated on vertically oriented planes; however, these nor the horizontally oriented planes were planes of maximum obliquity at larger strains. It is noted that Budhu used different measurement locations for the dense and loose specimen and assumptions of a similar stress state derived from measurements taken on the Cambridge DSS device because the stress state was not available for the NGI DSS device. Further analysis of this stress state for loose and dense granular materials using numerical techniques can bring additional insight to these findings.

For granular materials, discrete element method (DEM) simulations have provided useful insight into the particle-scale mechanics driving the observed overall response and have been particularly advantageous for studying granular soil response in laboratory element tests [13, 21, 30, 31, 43]. These simulations allowed examination of the particle-scale interactions, while also providing detailed information on the interaction of the test boundaries with the specimen. DEM simulations have also previously been used to study DSS devices in both two-dimensional [1, 37] and three-dimensional conditions [3, 14-16, 26, 44]. Wijewickreme et al. [44] examined the mobilized friction angle during shearing using simulations of a laminar ring NGI-type DSS apparatus under drained and constant volume conditions. For the drained specimen considered at low strains (< 5 %), they showed that the stresses on the horizontally oriented planes are close to the maximum shear stress, while at large shear strains (20 %) the lateral stresses continue to increase moving the stress state on the horizontally oriented plane closer to that of maximum stress obliquity. Asadzadeh and Soroush [3] conducted a similar DEM simulation in a laminar ring DSS device and concluded that the horizontal plane should be considered to be the plane of maximum shear stress at the peak shear stress, and after peak the stress state moves closer to maximum stress obliquity.

While these studies provided particle-scale data and insight into DSS, it is unclear how some modeling assumptions and boundary conditions may have affected the results. Dabeet [15], and Asadzadeh and Soroush [3] used glass beads in their laboratory testing and calibrated the DEM stiffness parameters through parametric studies. For example in Asadzadeh and Soroush [3], the Young's Modulus was reported as 40 GPa for the glass beads, but 100 MPa was used in the simulations to better match the experimental results. Also, while nominally spherical, glass ballotini may have irregular shapes [11] they may lead to issues in the direct comparison of experiments and DEM simulations comprised of perfect spheres; such shape anomalies are evident in the images provided by the photographs in Asadzadeh and Soroush [3]. In addition, inter-particle friction values larger than those reported for glass ballotini were used by Asadzadeh and Soroush [3] and Wijewickreme et al. [44]. This adjustment of the model parameters means that the simulations were calibrated against the experimental data, but parameters were varied simultaneously and thus the experiments do not strictly validate the model set-up. In the DEM-experimental comparison by Dabeet [15], a large physically unrealistic friction coefficient (10) was used for the particle-boundary interaction and the wire-reinforced membrane used in the experiments was simulated by using a stack of rings which moved to achieve a uniform boundary shear strain. While Dabeet [15] effectively matched the experimental stress-shear deformation response, the vertical strains associated with specimen compression during shear differed substantially.

Additionally, none of these earlier studies considered density effects: Asadzadeh and Soroush [3] considered only one vertical stress level and packing density; while Dabeet et al. [14] varied both contact stiffness and density, hindering isolation of density effects. It is unclear whether their conclusions will hold true at different densities. Wijewickreme et al. [44], Dabeet et al. [14], and Asadzadeh and Soroush [3] also analyzed internal stresses only and did not compare them with the boundary derived stresses that would be available in typical experimental tests. It is unclear whether their findings also hold true based on boundary measurements and whether they can be used by experimentalists to interpret laboratory test results. This study addresses these remaining questions and it serves as one of the few studies where the DEM particle geometries and input parameters closely match the physical laboratory specimen used. By using a DEM model that has been accurately validated against carefully controlled laboratory tests on spherical steel ball bearings (both particle properties and stress-strain and volumetric response), the model can be used with confidence to examine the internal stress state and boundary-derived stresses for specimens at two different densities.

LABORATORY VALIDATED 3D DEM SIMULATIONS

In a previous study by the authors, a new approach for simulating DSS test boundary conditions was implemented and was experimentally validated using laboratory tests on specimens of precision steel ball bearings. The three dimensional Particle Flow Code (PFC3D) by Itasca Consulting Group, Inc. [22] was used as the computational platform for the DEM simulations. While full details of the validation are provided in Bernhardt et al. [4], an overview is provided here to contextualize the analysis of the DEM-generated particle scale data presented below. It is noted that the numerical simulations aimed to replicate the laboratory experiments as closely as possible, therefore, they are described here concurrently.

The cylindrical laboratory and numerical specimens were approximately 28 mm in height and had a diameter of 101.6 mm, resulting in a diameter to height ratio sufficient to limit the non-uniformities to the extreme edges of the specimen [20, 41, 42]. The specimens consisted of a total of 60,000 spheres with equal quantities of three different sphere diameters (1.2 mm, 1.6 mm, and 2.0 mm). These particle diameters were shown to give a sufficient number of particles across the height of the specimen as discussed in Bernhardt et al. [4]. Precision chrome steel ball bearings were used in the laboratory specimens while spheres with the same size tolerances and material properties as the ball bearings were modeled in the DEM simulations. Similar steel spheres have been used in numerous experimental studies to advance understanding of granular material behavior [36, 37, 39, 49] dating back to the early studies by Wroth [49] and Rowe [37]. The clear advantages in using these here were: 1) the size, sphericity, and material properties of the ball bearings are consistent and can be experimentally determined and used in the DEM models directly, 2) the sphere-sphere contacts can be well captured in the DEM models by the Hertz-Mindlin contact model [11], and 3) the laboratory results can be directly compared to validate the DEM models comprised of assemblies of smooth spheres.

A latex membrane surrounded by a stack of 35 thin rings with a low-friction coating were used to confine the laboratory specimen, while 10 cylindrical rigid ring walls were shown to be suitable for the DEM simulations based on parametric studies conducted in Bernhardt et al. [4]. While the latex membrane was not directly introduced in the simulations, the frictional resistance between the sphere-membrane contact was modeled. Replicating the boundary conditions as closely as possible is important for boundary value problems like simple shear and Bernhardt et al. [4] showed that the boundary friction influenced the response and should be considered. The DEM simulation input parameters are listed in Table 1. The friction values were experimentally determined using particle-scale experiments. Specifically, the inter-particle friction value of the steel spheres was experimentally determined using an apparatus described in Cavarretta et al. [11]. No local damping or viscous damping was used. Coulomb (i.e., sliding) friction was used in the

DEM simulations to represent the measured physical friction (where the coefficient, $\mu_c = \tan\phi_u$ given in Table 1). No rolling friction was used as the steel spheres have a sphericity of one. The simplified Hertz-Mindlin contact model was used for all contacts in the simulations. The simplified Hertz-Mindlin model is a nonlinear contact formulation applicable to spheres in contact and it has been shown to capture the sphere-sphere contact for the precision ball bearings used in the physical experiments [11]. In PFC3D, only the shear modulus and Poisson's ratio are required to calculate the contact normal secant stiffness and the contact shear tangent stiffness using the geometric and material properties of the two entities in contact. The contact normal secant stiffness is given as

$$K^n = \left(\frac{2\tilde{G}\sqrt{2\tilde{R}}}{3(1-\tilde{\nu})}\right)\sqrt{U^n}$$

where $U^n$is the sphere overlap, $\tilde{R}$ is the effective radius, G is the effective shear modulus, and ν is the effective Poisson's ratio. For sphere-to-sphere contacts these properties are defined as

$$\tilde{R} = \frac{2R^{[A]}R^{[B]}}{R^{[A]} + R^{[B]}}$$

$$\tilde{G} = \frac{1}{2}\left(G^{[A]} + G^{[B]}\right)$$

$$\tilde{\nu} = \frac{1}{2}\left(\nu^{[A]} + \nu^{[B]}\right)$$

and for wall-to-sphere contacts the properties of the sphere is used. In the simplified Hertz-Mindlin contact model, a sliding condition is invoked once the tangential force equals the product of the normal force times the Coulomb friction coefficient. More details of the contact model and Coulomb friction including equations and assumptions can be found in the PFC3D manual [22]. Dry pluviation was used to prepare the laboratory specimens and the DEM specimens were similarly generated using gravity deposition.

The boundary algorithm implemented for this study considered stress transmission at the top and bottom horizontally oriented specimen boundaries and control of the radial confining rings. In the actual experiments a layer of particles were attached to the porous stones using high-strength epoxy to minimize slippage at the top and bottom horizontally oriented boundaries and ensure more uniform stress conditions. This fixed-particle boundary was modelled in the DEM simulations by setting the velocity of the particles contacting the top and bottom boundaries equal to the boundary velocities and by not allowing them to rotate (Fig. 2). Not only did this approach minimize slippage, it ensured that the top and bottom cap boundary conditions in the simulations were the same as those used in the laboratory. To replicate the laboratory loading conditions during shearing, the bottom wall in the DEM simulation (i.e., bottom specimen cap) was specified to move horizontally at a constant velocity and the top wall (i.e., top specimen cap) was maintained at a constant vertical stress using a servo-control algorithm (top wall was moved vertically to maintain the target stress). The laboratory specimen was sheared at a strain rate of 1.4 mm per hour, while the DEM specimen was sheared much slower to maintain quasi-static conditions. The quasi-static conditions were confirmed by ensuring that the maximum inertial number (5.1e-05) was significantly smaller than the threshold of 2.5e-3 proposed by Lopera Perez et al. [27]. The confining rings in the laboratory device in this study (and in most DSS devices in general) moved freely in response to the specimen deformation. In previous studies, researchers have specified a uniform shear strain on the radial boundary to impose simple shear conditions on the specimen by translating rings a specified distance or rotating a cylindrical confining wall [3, 15, 44]; however, in the actual laboratory tests the strain profile can deviate from these uniform boundary shear strain conditions at large strains. Therefore, to replicate the laboratory conditions more closely, a customized algorithm was developed that updated the position of the confining rings based on the target of a zero net force from the particles. This algorithm was necessary because in the DEM software used, the walls are boundaries whose position is controlled, rather than discrete bodies whose equilibrium is considered in the simulation. For the simulations, the main outputs recorded included: wall locations, particle-wall contact forces, particle locations, particle-particle contact forces, and particle rotational velocities. The laboratory data consisted of specimen cap locations (e.g., vertical location of the top cap and horizontal location of the bottom cap measured using displacement transducers), and vertical and shear forces measured by load cells located near the top and bottom specimen caps. The stress-strain and volumetric data captured from these tests was used to validate the numerical results.

Representative validation data for the specimens sheared are provided in Fig. 3. Designations D-100 and L-100 are used to describe the packing state of the specimen (i.e., 'D' for dense and 'L' for loose) and the magnitude of the constant vertical effective stress during testing (100 kPa for the results shown herein). Because the particles are spheres with a very low inter-particle friction, the range of densities in which specimens can be consistently prepared is rather limited and is lower overall than other granular geomaterials [12]. The experimental specimen maximum and minimum void ratios were 0.596 and 0.681, respectively as determined by ASTM D4253 and ASTM D4254. The initial void ratios (at 100 kPa) for the DEM and experimental specimens tested are provided in the legend of Fig. 3. Table 2 summarizes the initial void ratios once installed in the device (at approximately 10-15 kPa) and once loaded to a vertical effective stress of 100 kPa for each test, and the corresponding relative densities, R_D, based on the experimentally determined minimum and maximum void ratios. Note that for these specimens, a difference in specimen height of only 0.1 mm resulted in a difference in R_D of approximately 7%. While a range of densities were examined experimentally, only the loosest possible state (L) and the densest possible state (D) are considered here, as they were the most reproducible and provided a consistent comparison between the experiments and the DEM simulations. The aim was also to produce specimens whose initial states would be on either side of the critical state line to allow examination of both dilative and contractive responses, which was in fact exhibited by the D-100 specimens (dilative) and the L-100 specimens (contractive).

Overall, the stress-strain and volumetric responses of the dense and loose DEM specimens are in good agreement with the responses measured in the experimental tests. These numerical predictions are solely based on the input of independently measured material properties and inter-particle friction coefficients. No calibration procedure was employed to fine-tune input parameters which would produce the measured macroscopic response. Slight variations in peak stress and volumetric strain exist for the loose specimens, which is likely due to the small difference in initial void ratios. Although the initial void ratios are the same for the dense specimens, the initial stiffness is much higher for the DEM specimen (DEM D-100) compared to the experimental tests (D-100). The more dilative behavior is also a result of this stiffer initial condition, which was due to the specimen generation techniques. Further explanation of the specimen generation and its effects on the response can be found in Bernhardt et al. [4]. Even with the higher initial stiffness, the peak stress and the response beyond 5 % shear strain are well captured in the DEM simulation, thereby validating the results presented. Therefore, the results are fully and directly comparable, providing confidence that the underlying mechanisms of deformation and strength development are captured.

Although the results of only two DEM simulations are presented here for clarity, the conclusions are based on similar observations from six simulations and over 30 experimental tests encompassing a range of densities, two different stress levels (50 and 100 kPa) and two different particle size to specimen size ratios. Further details of the validation study which considered different stress levels and sample sizes are discussed in Bernhardt et al. [4]. Note that the remaining discussion and findings are based on observations from the DEM simulations.

STRESS TRANSMISSION IN SIMPLE SHEAR

Internal and Boundary Measurements of Stress and State Parameters

A non-uniform stress distribution is expected to form across the top and bottom horizontally oriented boundaries due to the inability of the DSS device to apply complementary shear stresses to the radial face of the specimen. Fig. 4 considers the distribution of the normal effective stresses on the top cap. Fig. 4(a) defines the leading and trailing edges relative to the direction of shearing. Fig. 4 (b) illustrates the particle contacts on the top cap of specimen D-100 at a boundary shear strain, $\gamma_{xz} = 1\%$ where the size of the circle is proportional to the magnitude of the vertical component of the contact force. A concentration of larger circles (i.e., higher compressive forces) can be seen on the leading edge of the specimen top cap. Figs. 4(c) and (d) consider the vertical effective stresses calculated for 16 equal slices (slice thickness is 3 times the maximum particle diameter) across the specimen for D-100 and L-100, respectively. Similar to the previous findings of Roscoe [35], Lucks et al. [28], and Budhu [7], the leading edge of the specimen experiences compression, while the trailing edge clearly experiences extension. Although there are non-uniformities, the stresses are relatively uniform throughout the central portion of the specimens.

In addition to non-uniformities along the boundaries, a number of previous experimental studies [7, 8, 45] and numerical studies [10, 28, 38] showed that the stress conditions within the specimen differ from those on the horizontally oriented specimen boundaries. To capture internal localized measurements of stress, five measurement spheres were placed within the specimen (Fig. 5). Measurement spheres are virtual measurement volumes over which average stresses, porosity, and many other quantities can be calculated and recorded as detailed in Potyondy and Cundall [32]. The diameter of the measurement spheres was chosen so that they provided a sufficient number of particles to give a representative volume, but remained at least two times the maximum particle diameter away from the boundary to minimize boundary effects arising from flat boundaries (i.e., lower density where spheres contact flat boundary walls) [4, 30]. Their locations were chosen to provide different representative measures of the internal stresses throughout the central portion of the specimen, and mimicked a similar load cell arrangement in Budhu [7]. Conditions in the central measurement sphere (M.S. 1) were considered to represent the stresses within the specimen core, while the average of all five measurement spheres represents the stresses within the central zone of the specimen. Note that average values were also calculated for the entire assembly (taken inside the boundaries to remove boundary effects) and the results were similar to that observed in the central zone. Fig. 6 presents comparisons of the vertical effective stress and shear stress calculated for the boundary and within the specimen core and central zone of the DEM specimen for simulations D-100 and L-100. In the DEM simulations, the vertical effective stress was calculated from force measurements taken on the top boundary, while the shear stress was calculated from force measurements taken on the bottom boundary. This replicated the measurement locations in the experimental apparatus used in this study (and many typical NGI-type DSS devices); however, equivalent measurements were similar on both boundaries. For both specimens, the core is clearly under higher normal stresses than what is observed on the top horizontal specimen boundary (Figs. 6(a) and 6(b)). As discussed in Bernhardt et al. [4], the higher stress observed in the central core is likely due to the fact that the density is higher in this region.

This stress difference is also directly in line with experimental findings presented previously in the literature [7, 8, 45].

According to the simulations, vertical effective stresses derived from the top boundary underestimate the vertical effective stresses within the specimen core by approximately 10% and within the central zone by approximately 8% in both specimens. The shear stresses observed on the boundary, however, are mostly representative of the shear stresses within the specimen. Discrepancies can be seen for the dense specimen, referring to Fig. 6(c), where the boundary-derived stresses underestimate the shear stresses in the specimen core by roughly 7% until approximately 9% shear strain. When the shear stress is normalized by the vertical effective stress and stress ratio is plotted, the boundary based stress ratios overestimate the stress ratios experienced within the specimen core and central zone of D-100 by roughly 5% and 8%, respectively (Fig. 7 (a)). The stress ratio calculated on the boundary of L-100; however, is representative of the stresses at all locations within the specimen (Fig. 7 (b)). Therefore in practice, boundary measurements may provide unconservative estimates of peak stress ratio for dense materials. The difference between the boundary stresses and the internal stresses in the core observed for the dense specimen also has implications for DEM analysts who often use stress derived from a measurement sphere in the specimen core (similar to M.S. 1) in servo-controlled algorithms to control the consolidation stress and the stresses during testing.

Failure State

As discussed, in the NGI-type DSS devices the principal stresses and thus the Mohr's circle at failure cannot be determined experimentally without making some assumptions. In contrast, the complete stress state is available in the DEM simulations and these assumptions can be critically analyzed. The central zone of the specimen is considered here to avoid the boundary effects. As shown previously, the central zone is also under uniform stress conditions and encompasses a large portion of the total specimen volume, providing a valid assessment of average stresses to compare with the observed boundary response.

Fig. 8 compares the normal effective stresses in the central zone in both specimens. For the dense specimen, the normal effective stress on the vertical plane in the direction of shearing (σ'_{xx}) increases during shearing and exceeds the normal effective stresses on the two orthogonal planes. The normal effective stress on the vertical plane also increases during shearing in the loose specimen; however, the normal effective stresses on the horizontal plane (σ'_{zz}) remain larger throughout.

Shear stress ratios within the central zones of the specimens on the vertical plane (τ_{xz}/σ'_{xx}) and horizontal plane (τ_{zx}/σ'_{zz}) were also examined (Fig. 9). Although there is some noise in the curves, the shear stress ratios on the vertical plane in both specimens reach their maximum (represented by point A) before those on the horizontal plane attain a maximum value (represented by point B). For strain levels exceeding γ_{zx}=2% in D-100, the shear stress ratio on the horizontal plane exceeds that on the vertical plane. After the maximum shear stress ratio is reached on the horizontal plane (at approximately γ_{zx}=9.2%), it reduces slightly and once again becomes equal to the shear stress ratio on the vertical plane at the maximum shear strain imposed in this study (represented by point C). For L-100, the maximum shear stress ratio on the vertical plane is reached at much higher shear strains (represented by point A at approximately γ_{zx}=12.6%) and the point at which the stress ratios on both planes become equal does not occur until even higher shear strains (near the end of the test at approximately γ_{zx}=14.8%). The two shear stress ratios then remain approximately constant and equal through the rest of the test. Therefore, the maximum shear stress ratio on the horizontal plane (represented by point B) corresponds to the shear stress ratio at the maximum shear strain imposed in this study and no reduction is observed for L-100 (i.e., point C is essentially the same as point B).

Figs. 10(a) and (b) illustrate the Mohr's circles based on the average stresses within the central zone of the specimens for various stages during the tests on the loose and dense specimens respectively. In both cases, the initial state after K_0 consolidation (γ_{zx}=0%) is shown with a solid Mohr's circle. Mohr's circles for other relevant times during the test (similar to Fig. 9) are also shown: the point at which the maximum shear stress ratio on the vertical plane is reached (A), the point at which the maximum shear stress ratio on the horizontal plane is reached (B), and the point at which the shear stress ratios on the vertical and horizontal planes are equal (C), corresponding also to the end of the test. As illustrated in Fig. 10(b) for L-100, the Mohr's circles for stages B (maximum shear stress ratio on horizontal planes) and C (shear stress ratio on horizontal planes becoming equal to the vertical), coincide, reflecting the discussion regarding Fig. 9.

Budhu [9] also showed the shear stress ratio on the vertical plane initially exceeds that on the horizontal plane and reaches its maximum first. The associated Mohr's circles depicted the vertical planes as planes of maximum stress obliquity, leading to the hypothesis that failure is initiated on these planes, where the stress ratio then remains constant in a state of continuous failure, which Budhu also identifies as critical state. The results in Fig. 10 show the point of maximum stress ratio on the vertical plane (A) does not correspond with maximum obliquity in either the dense or loose specimen and the tangency point represents a plane slightly inclined from the horizontal. Following de Josselin de Jong's 'book-stack' hypothesis, it is still likely that shearing on the vertical planes is initially kinematically easier (the particles can move more easily in the vertical direction than in the horizontal direction). However, according to the DEM results here, the vertical plane is never a failure plane during any phase of the test, if failure is interpreted both as maximum (peak) or minimum (critical state) resistance and according to the Mohr-Coulomb tangency hypothesis. While at some point during the test the maximum obliquity occurs on the vertical plane, the second condition is not satisfied because the stress state is still growing. Softening of the shear stress ratio on the vertical plane (τ_{xz}/σ'_{xx}) is small for the specimens considered here, so that maximum obliquity on this plane seems to represents a minimum limiting condition and can be, therefore, along with Budhu [9], interpreted as critical state. Budhu [9] shows a more pronounced softening of the shear stress ratio on the vertical plane compared to what was observed in this study. The lack of marked strain softening may be due to the perfectly spherical particles used here and their very low corresponding inter-particle friction value, unlike in Budhu's study where the results were obtained from tests on sand with more angular particles. Work by Wijewickreme et al. [44] and Asadzadeh and Soroush [3] also support this interpretation, as they used spheres with higher inter-particle friction values. In their cases, the minimum strength is reached on the vertical planes more slowly once the stress ratio decreases to its minimum value at the end of the test.

The horizontal effective stress (σ'_{xx},), which is not controlled in either the physical tests or the simulations, increases with shearing (Fig. 8) due to the rotation of the principal stresses and kinematic constraint imposed by the rigid boundary rings which prevent radial deformations. As shearing progresses, the complementary shear stresses acting on both vertical and horizontal planes continue to increase; consequently the normal horizontal stress must increase, while the shear stress ratio on the vertical plane remains at the minimal, critical state, condition (or decreases slowly). The stress state on the vertical plane, then, slides along the critical state condition. At the same time, the shear stress ratio on the horizontal plane continues to rise, since the normal vertical stress is maintained constant. The maximum overall obliquity in the specimen is achieved when the shear stress ratio acting on the horizontal plane is largest, but the two are not the same.

For dense specimens, the shear stress ratio on the horizontal plane surpasses that on the vertical plane and continues to grow until it reaches a maximum at point B. The principal stresses have now rotated considerably (the major principal stress is oriented at 47.3° from the vertical in Fig. 10(a)) and the friction angle is ϕ'_B with maximum obliquity, or failure, occurring on a plane slightly inclined to the horizontal. Assessment of these angles is not possible when the normal horizontal effective stress is unknown, without making some assumption (see [45]). The results show that the condition of maximum obliquity, even if reached at the peak horizontal effective stress, does not occur on the horizontal plane, but the difference between the two conditions is quite small, and seems even smaller in the results presented in Wijewickreme et al. [44] and Asadzadeh and Soroush [3].

Under continued shearing the shear stress ratio on the horizontal plane for D-100 then decreases to the value of that on the vertical plane, causing the Mohr's circle to shrink back from its maximum size, ultimately to C, when the conditions on both planes reach critical state. For loose specimens, the peak shear stress ratio on the horizontal plane is reached at very high strains and corresponds to the maximum shear strength of the specimen.

The principal stresses in the central zone can be obtained by eigenvalue decomposition of the stress tensor, allowing the angle of shearing corresponding to the maximum obliquity to be directly calculated as

$$\phi' = \sin^{-1}\left(\frac{\sigma'_1 - \sigma'_3}{\sigma'_1 + \sigma'_3}\right) \quad (1)$$

This value of ϕ' can be compared to the angles of shearing resistance determined for the three common failure assumptions discussed previously (Fig. 11). Assumption 1 refers to the assumption that the horizontal plane is the plane of maximum obliquity. Assumption 2 says that the horizontal planes are planes of maximum shear stress, and Assumption 3 is that vertical planes are planes of maximum obliquity. Each of these calculations use stresses derived from internal measurements for the central zone of the specimen.

Although it is difficult to see on the full-scale plot, the detail in Fig. 11(a) shows that ϕ' for the dense specimen is initially closest to the angle of shearing resistance calculated based on the assumption that failure initiates on the vertical plane (Assumption 3) and then quickly crosses to the angle calculated based on the assumption that the maximum shear stress acts on the horizontal plane (Assumption 2) as the shear stress ratios on the two planes cross. The calculated friction angle then remains almost constant between the values for Assumptions 1 and 2 because both the Mohr's circle growth and the principal stresses rotation slow. The friction angle is close to the value for Assumption 1, but it never exactly reaches it, indicating that the horizontal plane is never the plane of maximum obliquity and the actual failure plane is inclined at a very small angle to the horizontal, confirming the experimental observations by Roscoe et al. [35] and Airey et al. [2]. The difference between the actual peak friction angle and that derived from Assumption 2 at peak conditions is relatively small in this case, which is likely due to the fact that there is minimal softening. Eventually, at the very end of the test, the friction angle reaches Assumption 2, indicating stress ratios on both planes are at a critical state. This differs from the conclusions drawn by both Asadzadeh and Soroush [3] and Wijewickreme et al. [44]. For L-100 (Fig. 11(b)), the calculated angle of shearing resistance is closest to the angle for the assumption that failure occurs on the vertical plane for the majority of shearing, until at very large strains the angle calculated based on Assumption 2 becomes closest. When this condition is met, the horizontal effective stresses and the shear stress ratio on the vertically oriented plane are still increasing, putting into question whether actual failure is occurring for this specimen.

Fig. 12 illustrates the orientation of the major principal stress from vertical, α, calculated directly for the central zone of the DEM specimens. As expected, the principal stress axis rotates smoothly during shearing and the magnitude and rate of the rotation are density dependent (i.e., D-100 shows a much faster rate of rotation than L-100). In both specimens, the orientation of the major principal stress approaches 45° at large strains, indicating that the horizontal and vertical planes eventually become planes of maximum shear stress (i.e. failure Assumption 2).

The ϕ' directly calculated in the central zone of the specimen was also compared with the ϕ' calculated for Assumptions 1 and 2 using the measurements taken on the horizontally oriented specimen boundary (Fig. 13), as would be available in actual physical tests. For the loose specimen (Fig. 13(b)), the friction angle can be confidently estimated considering the maximum shear stress acting on the horizontal plane, which is easily inferred during the physical test from the measured shear force. However, this is not true for the dense specimen (Fig. 13(a)). While Assumption 1 is a close approximation at large strains it is not as good of an estimation at peak conditions. Based on internal measurements of stress, Asadzadeh and Soroush [3] and Wijewickreme et al. [44] concluded that Assumption 2 is appropriate at peak conditions and Assumption 1 is appropriate at large strains, but this does not extend to the case when boundary measurements are used. It is clear that using boundary data and either assumption to derive the friction angle can be misleading and that no single assumption describes the behavior at all strains or densities.

PARTICLE DISPLACEMENTS DURING SHEARING

The DEM simulations were further analyzed to examine the particle displacements within the specimen. Figs. 14-16 present the particle displacements in the three coordinate directions occurring from 0 to 15% shear strain plotted as a function of their vertical positions within D-100 and L-100. The dashed black lines represent the linear variation in displacement obtained from the displacement of the boundary walls. The solid line in Fig. 14 represents a linear fit to the particle displacements throughout the middle two-thirds of the specimen and was used to examine the portion of the specimens that exhibited a linear displacement profile (i.e., uniform simple shear). Fig. 14 shows that the particle displacements follow the curved trend resembling observations made by Finn et al. (1971) using plasticene samples. While the boundary effects are clearly seen, it is difficult to conclude whether the distortions are greater due to the fixed-particle boundary used in this study, although it is likely that any type of shear transmitting caps would present similar profiles. The high R^2 value associated with the best fit line through the middle particles shows that this portion of the specimen is deforming in simple shear with a higher shear strain than what one would infer from the boundary measurements.

An interesting feature of granular material behavior is the out of plane displacements which occur during shearing even though the direct simple shear test is considered to be a plane strain test. Fig. 15 presents the incremental horizontal displacements in the y-direction (out of plane from the shearing direction) as a function of the vertical position of the particles. Both specimens contain a finite number of particles which move out of plane during shearing (by a measurable amount when compared with the horizontal displacements illustrated in Fig. 14). It is clear that the L-100 specimen has a greater number of particles with relatively large out of plane displacements. This indicates that particles within the L-100 specimen could rearrange laterally without the need for dilation which agrees with the contractive macro-response observed.

In the simulations considered the D-100 sample dilated approximately 0.609 mm and the L-100 specimen contracted 0.036 mm over the shear strain interval of $\gamma zx=0\%$ to $\gamma zx=15\%$. Fig. 16 illustrates the incremental vertical displacements as a function of vertical position within the samples. In both specimens, the range of z-displacements of the particles throughout the middle two-thirds of the specimens is larger than in other regions, indicating greater rearrangement within this zone. D-100 had a finite number of particles which moved downwards during shearing (displacement < 0), even though the sample as a whole dilated upwards. The maximum particle displacements (1.2 mm both upwards and downwards) were approximately twice the vertical displacement measured on the top boundary of D-100. Although the vertical displacement of the top boundary was small in L-100 (-0.04 mm), the particles exhibited both positive (1.41 mm) and negative (-2.32 mm) vertical displacements which were greater than the displacements observed in D-100, indicating that the particles experience greater rearrangement. The root-mean-square deviation (RMSD) from the interpolated boundary displacements was used to quantify the difference between the individual particle displacements and the vertical displacement of the top boundary. RMSD values of 0.17 and 0.21 were obtained for D-100 and L-100, respectively. These data further confirm that the particles within L-100 are able to rearrange without the need for global dilation, leading to a lower overall strength.

Vertical particle displacements (z-direction) were also plotted as a function of the horizontal position of the particles (Fig. 17). Fig. 17a shows the global dilation occurring in D-100 where the boundary particles are clearly seen as the concentration of particles forming the two visible lines and Fig. 17b shows the very slight global contraction where the boundary particles are more concentrated near zero. The leading edge (right) and the trailing edge (left) show a higher number of particles above and below the global displacements, respectively. These very closely relate to the normal stress distributions illustrated in Fig. 4 and it is further proof that the boundary conditions in the simple shear device lead to distortions at the specimen edges where particles may experience much higher rearrangement. The central zone of the specimen, however, exhibits a much more uniform response.

CONCLUSIONS

Validated DEM simulations of dense and loose specimens of an idealized granular material were used to examine the stress transmission, particle kinematics, and failure state in laminar-type simple shear devices under drained constant effective stress conditions. The following conclusions can be made:

1. The normal effective stresses calculated within the specimen core were observed to be much higher than those calculated for the specimen boundary. Shear stresses did not show such a marked difference, and the stresses derived from boundary measurements were quite representative of the internal stresses for central zone of the specimen.
2. Boundary measurements may provide unconservative estimates of peak stress ratio for dense specimens, however, they were shown to be good estimators for the loose specimen.
3. Because the horizontal stress is not controlled, the maximum shear stress ratio is reached at different strain levels on different planes. While the shear stress ratio rises initially faster on the vertical planes, these nor the horizontal planes were shown to be the planes of maximum stress obliquity at large strains. For both specimens in this study, softening of the shear stress ratio on the vertical plane (τ_{xz}/σ'_{xx}) is minimal compared to the softening

shown in Budhu [9]. This may be an indication of the effects of several key factors on the response, such as angularity, gradation, and interparticle friction, since his results were obtained from tests on sand, rather than smooth spheres.

4. In tests with no strain-softening (loose specimens), Assumption 2 is applicable at peak conditions, providing a correct estimate for the friction angle. This is true considering both internal stress states and boundary-derived stresses (as would be gathered in an experimental test). For dense tests with strain-softening, maximum obliquity is not reached on either vertical or horizontal planes and, therefore, none of the most common assumptions to interpret strength parameters in DSS tests is able to fully capture the peak friction angle. Assumption 2 is applicable based on the internal measures of stress; however, this assumption overestimates the friction angles when boundary measures of stress are used.
5. The metal ball bearings tested in this study have very low inter-particle friction values and spherical shape, which limit the development of significant peak shear strength followed by strain-softening even in their densest condition. The assumption that the maximum shear stresses act on the horizontal plane is representative of the failure state at large strain conditions for this material regardless of density. Thus, dense sands which have higher inter-particle friction values and more angular particle shapes are likely to exhibit larger peak strengths and may show a deviation from the conclusions made here.
6. The DEM data enable direct observation of the particle-scale kinematics of the specimen response. A non-negligible number of particles experienced finite displacements orthogonal to the direction of shearing in both samples considered; there is evidence of greater rearrangement within the loose sample. The vertical displacement data indicate a

greater amount of rearrangement within the middle 2/3 of the specimen. The variation in vertical displacements across the sample can be related to the vertical contact forces calculated along the sample boundaries.

ACKNOWLEDGMENTS

This material is based upon work supported by the National Science Foundation under Grant No. 0449021 and the Graduate Research Fellowship Program. Any opinions, findings, and conclusions or recommendations expressed in this material are those of the authors and do not necessarily reflect the views of the National Science Foundation. The authors also wish to acknowledge the support provided by the Zachry Department of Civil Engineering at Texas A&M University.

Conflict of Interest: The authors declare that they have no conflict of interest.

REFERENCES

1. Ai, J., Langston, P. A., Yu, H.S.: Discrete element modelling of material non-coaxiality in simple shear flows. Int. J. Numer. Analyt. Methods Geomech. **38(**6), 615-635 (2014)
2. Airey, D., Budhu, M., Wood, D.: Some aspects of the behaviour of soils in simple shear. Chapter 6 in Developments in soil mechanics and foundation engineering (eds P. K. Banerjee and R. Butterfield), Elsevier, London, UK, **2**, 185-213 (1985)
3. Asadzadeh, M., Soroush, A.: Fundamental investigation of constant stress simple shear test using DEM, Powder Technol. **292**, 129-139 (2016)
4. Bernhardt, M. L., Biscontin, G., O'Sullivan, C.: Experimental validation study of 3D direct simple shear DEM simulations. Soils Found. **56**(3), 336-347 (2016)
5. Bjerrum, L., Landva, A.: Direct simple shear test on a Norwegian quick clay. Géotechnique **16**(1), 1–20 (1966)
6. Budhu, M.: Simple shear deformation of sands." Ph.D. Thesis, University of Cambridge (1979)
7. Budhu, M.: Nonuniformities imposed by simple shear apparatus. Can. Geotech. J. **21**(1), 125-137 (1984)
8. Budhu, M.: Lateral stresses observed in the simple shear apparatus. J. Geotech. Geoenviron. Engng. **111**(6), 698-711 (1985)
9. Budhu, M.: Failure state of a sand in simple shear. Can. Geotech. J. **25**(2), 395–400 (1988)
10. Budhu, M., Britto, A.: Numerical analysis of soils in simple shear devices. Soils Found. **29**(2), 31–41 (1987)
11. Cavarretta, I., O'Sullivan, C., Ibraim, E., Lings, M., Hamlin, S., Muir Wood, D.: Characterization of artificial, spherical particles for DEM validation studies. Particuology **10**(2), 209-220 (2012)

12. Cho, G. C., Dodds, J., Santamarina, J. C.: Particle shape effects on packing density, stiffness, and strength: Natural and crushed sands. ASCE J. Geotech. Geoenviron. Engng. **103**(5), 591-602 (2006)
13. Cundall, P.A., Strack, O.D.L.: A discrete numerical model for granular assemblies, Géotechnique **29**(1), 47-65 (1979)
14. Dabeet, A., Wijewickreme, D., Byrne, P. M.: Discrete element modelling of direct simple shear response of granular soils and model validation using laboratory element tests. Proc. Pan-Am CGS Geotechnical Conference, Toronto, Canadian Geotechnical Society (2011)
15. Dabeet, A.: Discrete element modeling of direct simple shear response of granular soils and model validation using laboratory tests. PhD Thesis. University of British Columbia, Vancover (2014)
16. Dabeet, A., Wijewickreme, D., Byrne, P.: Evaluation of stress strain non-uniformities in the laboratory direct simple shear test specimens using 3D discrete element analysis, Geomech. Geoeng. **10**(4), 249-260 (2015)
17. de Josselin de Jong, G.: The double sliding, free rotating model for granular assemblies. Géotechnique **21**(2), 155-162 (1971)
18. Dounias, G.T., Potts, D.M.: Numerical analysis of drained direct and simple shear tests, Journal of Geotechnical Engineering **119**(12), 1870-1891 (1993)
19. Duncan, J. M., Dunlop, P.: Behavior of soils in simple shear tests, Proc. of The Seventh International Conference on Soil Mechanics and Foundation Engineering, **1**, 101-109 (1969)
20. Franke, E., Kiekbusch, M., Schuppener, B.: A new direct simple shear device. Geotech. Testing J. **14**(4), 190–199 (1979)

21. Huang, X., Hanley, K., O'Sullivan, C., Kwok, F. C. Y.: Effect of specimen size on the response of DEM specimens with a realistic grading. Particuology **15**, 107-115 (2014)

22. Itasca Consulting Group, Inc.: PFC3D - Particle flow code in three dimensions, version 4.0. Itasca Consulting Group, Inc., Minneapolis, MN, USA (2008)

23. Jardine, J. R., Menkiti, C. O.: The undrained anisotropy of k_0 consolidated sediments. Proc. ECSMGE, Amsterdam, The Netherlands **2**, 1101-1108 (1999)

24. Kammerer, A.: Undrained response of cohesionless soils under multidirectional cyclic simple shear conditions. Ph.D. Thesis, University of California, Berkeley (2002)

25. Kjellman, W.: Testing the shear strength of clay in Sweden. Géotechnique **2**(3), 225-232 (1951)

26. Langston, P., Ai, J., Yu, H.S.: Simple shear in 3D DEM polyhedral particles and in a simplified 2D continuum model. Granul. Matter **15**(5), 595-606 (2013)

27. Lopera Perez, J. C., Kwok, C.Y., O'Sullivan, C., Huang, X., Hanley, K.J.: Assessing the quasi-static conditions for shearing in granular media within the critical state soil mechanics framework. Soils and Found. **56**(1), 152-159 (2016)

28. Lucks, A., Christian, J., Brandow, G., Hoeg, K.: Stress conditions in NGI simple shear test. J. Soil Mech. Found. Div. ASCE **98**(SM1), 155-160 (1972)

29. Malek, A. M.: Cyclic behavior of clay in undrained simple shearing and application to offshore tension piles. Ph.D. Thesis, MIT (1987)

30. Marketos, G., Bolton, M.D.: Flat boundaries and their effect on sand testing. Int. J. Numer. Analyt. Methods Geomech. **34**(8), 821-837 (2010)

31. O'Sullivan, C.: Particulate Discrete Element Modeling. Spoon Press/Taylor & Francis, New York, NY (2011)

32. Potyondy, D.O., Cundall, P.A.: A bonded-particle model for rock. Int. J. Rock Mech. Mining Sci. **41(**8), 1329-1364 (2004)

33. Prévost, J.H., Hoeg, K.: Reanalysis of simple shear soil testing. Canadian Geotechnical Journal, **13**, 418-429 (1976)

34. Roscoe, K.: An apparatus for the application of simple shear to soil specimens. Proc. 3rd Int. Conf. Soil Mech. Found. Engng **1**, 186-191 (1953)

35. Roscoe, K., Bassett, R. H., Cole, E. R.: Principal axes observed during simple shear of a sand. Proc. Geotech. Conf., Oslo **1**, 231-237 (1967)

36. Roscoe, K. H., Schofield, A. N., and Wroth, C. P.: On the yielding of soils. Géotechnique, **8**(1), 22-53 (1958)

37. Rowe, P.W.: The stress-dilatancy relation for static equilibrium of an assembly of particles in contact. Proc. of the Royal Society of London. Series A, Mathematical and Physical Sciences, **269**(1339), 500-527 (1962)

38. Saada, A. S., Townsend, F. C.: State of the art: laboratory strength testing of soils. Laboratory shear strength of soils, ASTM Spec. Tech. Publ. **740**, 7-77 (1981)

39. Santamarina, C., Cascante, G.: Effect of surface roughness on wave propagation parameters. Géotechnique, **48**(1), 129–136 (1998)

40. Shen, C. K.: A micromechanical investigation of drained simple shear tests on dense sand using discrete element simulations. PhD thesis, Imperial College London, London, UK (2013)

41. Shen, C. K, Sadigh, K., Herrmann, L. R.: An analysis of NGI simple shear apparatus for cyclic load testing. Dynamic Geotech. Testing, ASTM International, No. STP 654, 148-162 (1978)

42. Stroud, M.: The behavior of sand at low stress levels in the simple shear apparatus." Ph.D. Thesis, University of Cambridge (1971)

43. Talesnick, M., Frydman, S.: Simple shear of an undisturbed soft marine class in NGI and torsional shear equipment. Geotech. Testing J. **14**(2), 180-194 (1991)
44. Vucetic, M.: The influence of height versus diameter ratio on the behaviour of Haga clay in the NGI simple shear device. Internal Report No.56204-9, Norwegian Geotechnical Institute, Oslo, Norway (1981).
45. Vucetic, M., Lacasse, S.: Specimen size effect in simple shear test. J. Geotech. Engng Div. ASCE **108**(2), 1567-1585 (1982)
46. Wang, J., Gutierrez, M.: Discrete element simulation of direct shear specimen scale effects. Géotechnique **60**(5), 395-409 (2010)
47. Wijewickreme, D., Dabeet, A., Byrne, P. M.: Some observations on the state of stress in the direct simple shear test using 3d discrete element analysis. Geotech. Testing J. **36**(2), 1-8 (2013)
48. Wood, D. M., Drescher, A., Budhu, M.: On the determination of the stress state in the simple shear apparatus. Geotech. Testing J. **2**(4), 211-222 (1979)
49. Wroth, C. P.: The behavior of soils and other granular media when subjected to shear. Ph.D. Thesis, University of Cambridge, (1958)

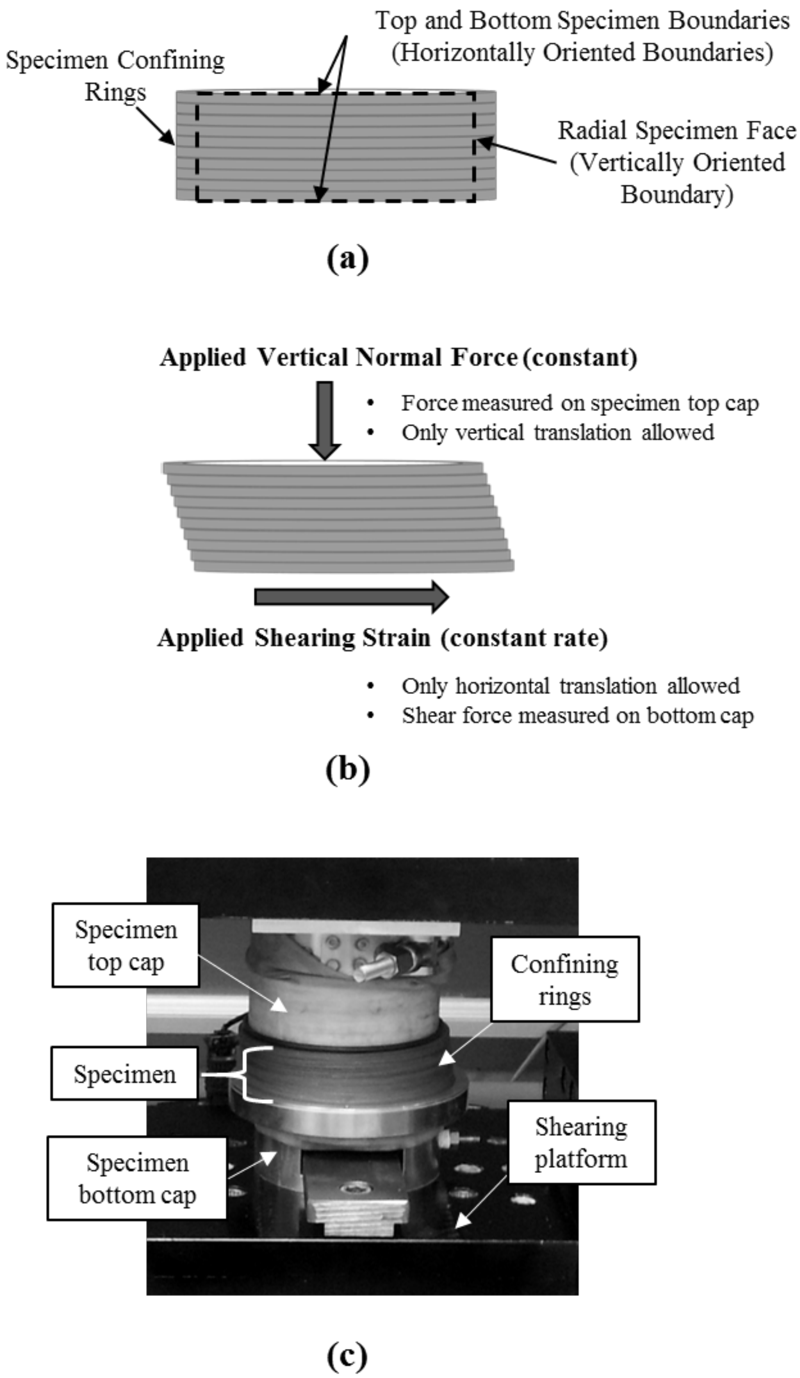

Fig. 1 a Schematic of cylindrical specimen detailing boundary terminology used herein, **b** Schematic of specimen describing loading scheme and measurement locations, and **c** Annotated photograph of laboratory specimen loaded in simple shear testing fixture.

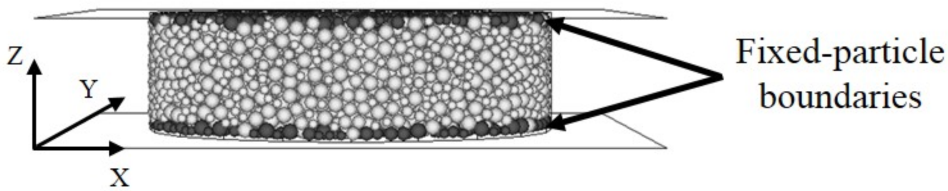

Fig. 2 DEM specimen showing fixed-particle boundary walls where the layer of particles contacting the top and bottom boundary (dark particles) are "virtually glued" to the boundaries by fixing their rotations to zero and their velocities equal to the velocities of the top and bottom specimen boundary walls.

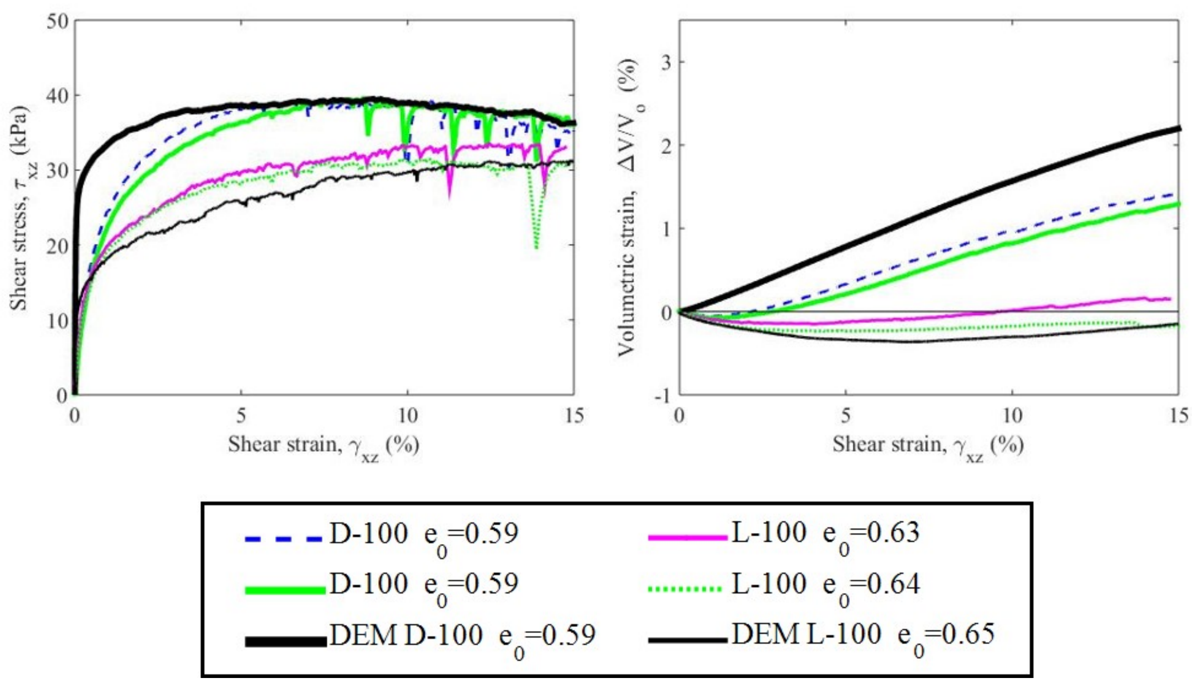

Fig. 3 Representative validation data for dense (D-100) and loose (L-100) specimens tested at a constant vertical effective stress of 100 kPa (after Bernhardt et al. [4]). Experimental tests conducted on precision steel spheres were used to validate DEM simulations of spheres.

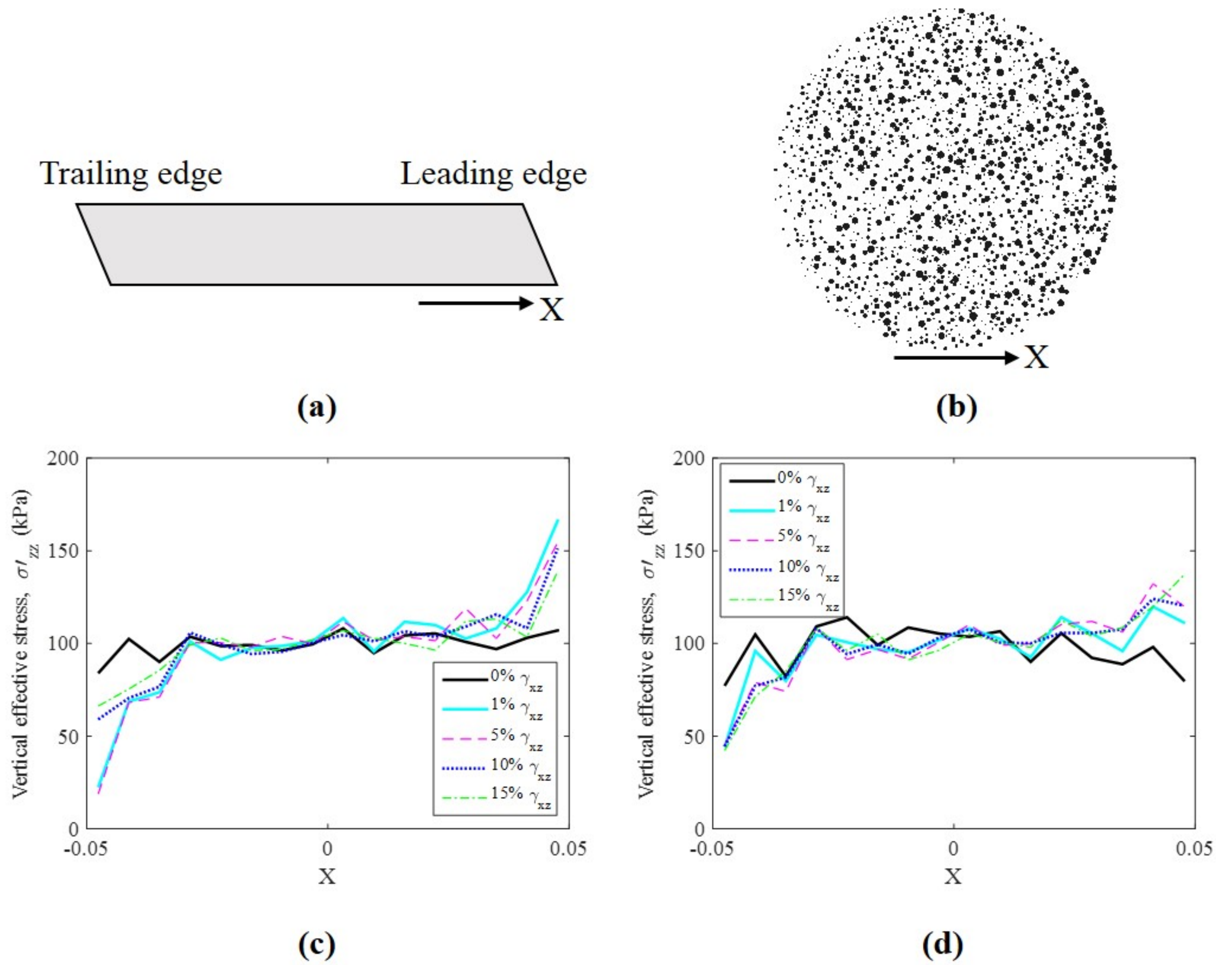

Fig. 4 **a** Schematic showing the shearing direction terminology used herein, **b** Plot of vertical contacts on the top cap for DEM specimen D-100 at γ_{xz}=1% (size of the filled circle is proportional to the magnitude of the vertical component of the contact force) showing a higher concentration of large contacts on the leading edge of the specimen, **c** Calculated vertical effective stress distribution on the top cap of DEM specimen D-100, and **d** Calculated vertical effective stress distribution on the top cap of DEM specimen L-100.

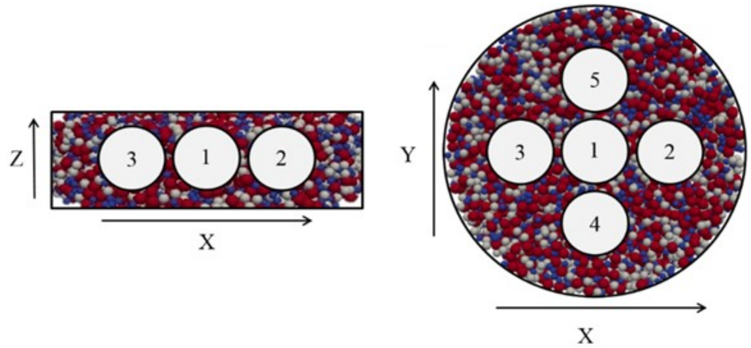

Fig. 5 Elevation and plan views of measurement sphere (M.S.) locations within the DEM specimens where M.S. 1 is considered the specimen core and the average of all five M.S. is considered the central zone of the specimen. The diameter of each M.S. is 23.4 mm and M.S. 2-5 are spaced 25.4 mm from the center of the specimen.

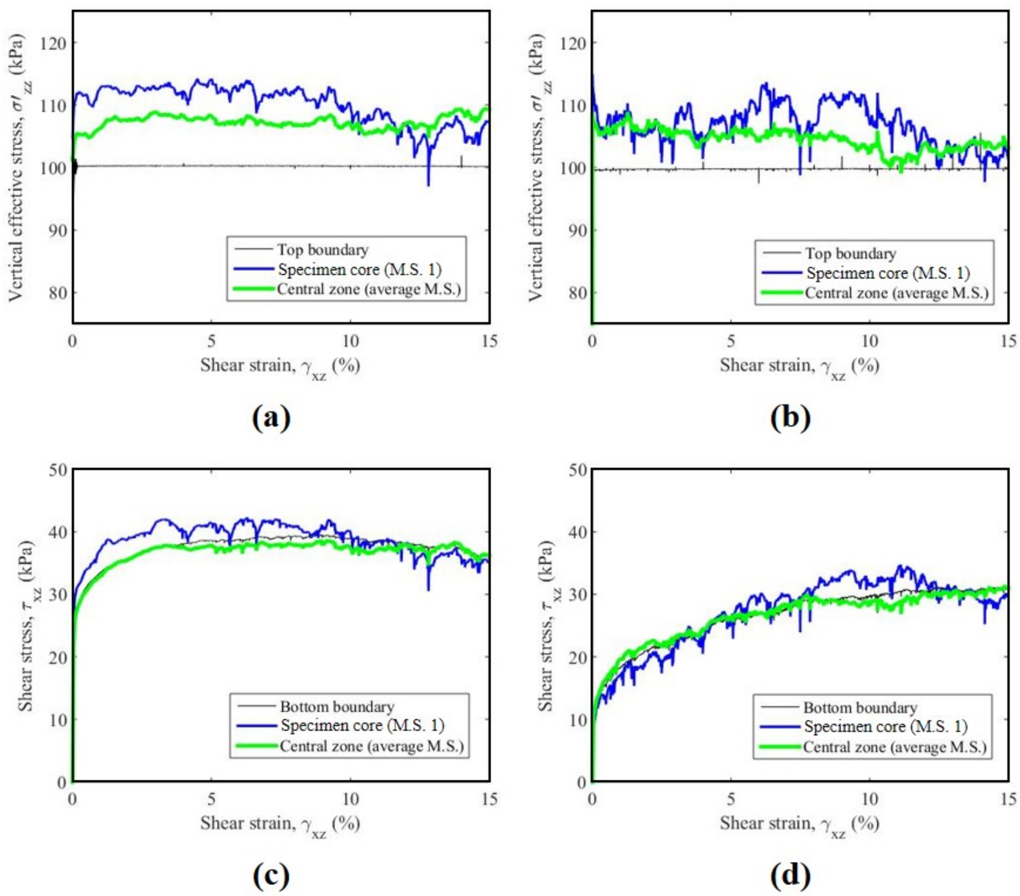

Fig. 6 Comparison of vertical effective stress and shear stress responses calculated at different locations of the DEM specimens for, **a** D-100 vertical effective stress, **b** L-100 vertical effective stress, **c** D-100 shear stress, and **d** L-100 shear stress.

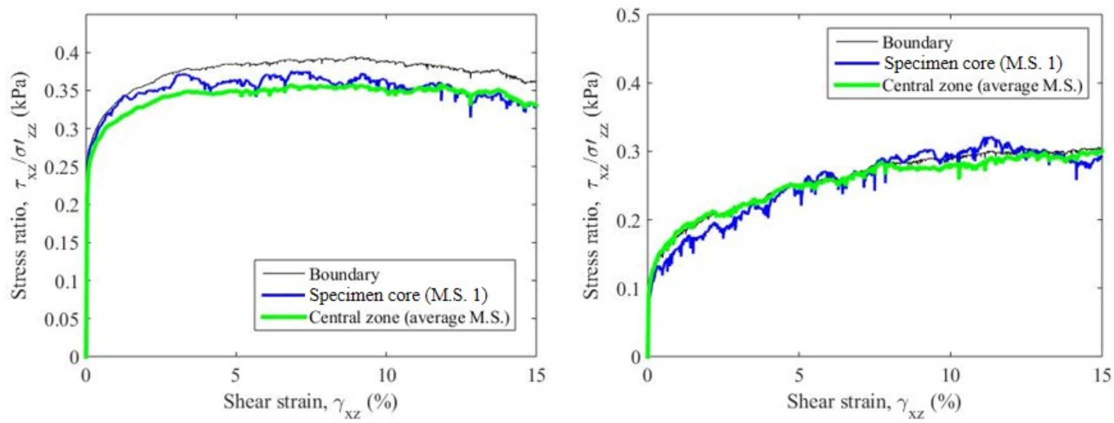

(a) **(b)**

Fig. 7 Comparison of stress ratio versus shear strain calculated at different locations of the DEM specimens for **a** D-100, and **b** L-100. Calculations of boundary stress ratio are based on measurements on the horizontally oriented specimen boundaries as available in routine DSS testing.

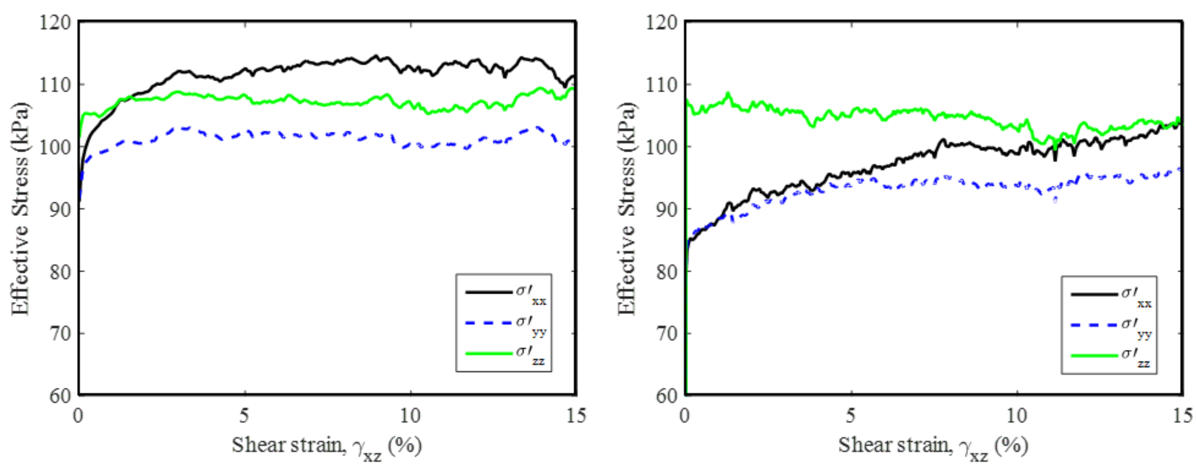

(a) **(b)**

Fig. 8 Comparison of normal effective stresses within the central zone of the DEM specimen for **a** D-100 and **b** L-100. Horizontal effective stress, σ'_{xx}, acts on vertically oriented planes, whereas vertical effective stress, σ'_{zz}, acts on horizontally oriented planes.

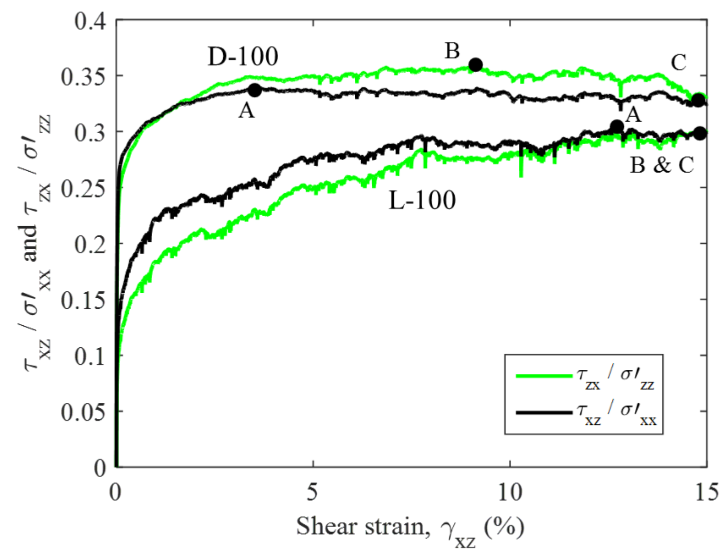

Fig. 9 Comparison of shear stress ratios on the vertical plane (τ_{xz}/σ'_{xx}) and horizontal plane (τ_{zx}/σ'_{zz}) within the central zone of the DEM specimen. Points labeled as A - the point at which the maximum stress ratio on the vertically oriented plane is reached, B - the point at which the maximum stress ratio on the horizontally oriented plane is reached, and C - the point at which the stress ratios on the vertically and horizontally oriented planes are equal.

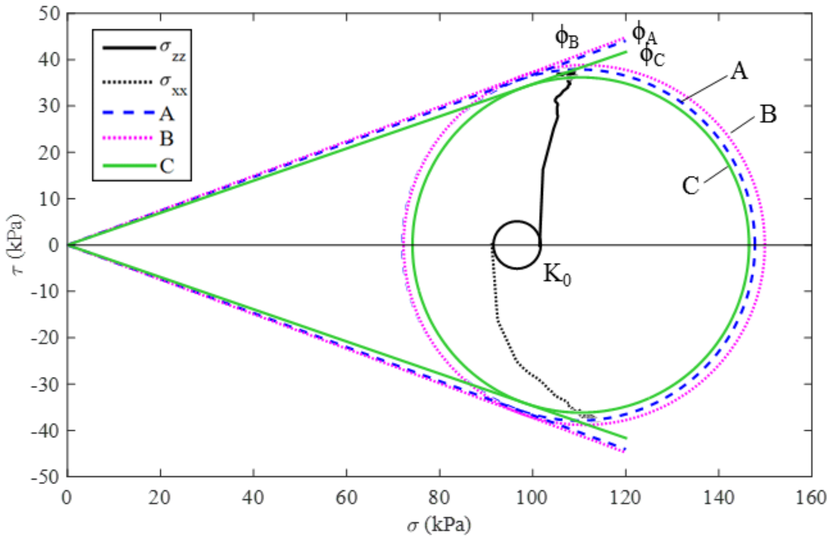

(a)

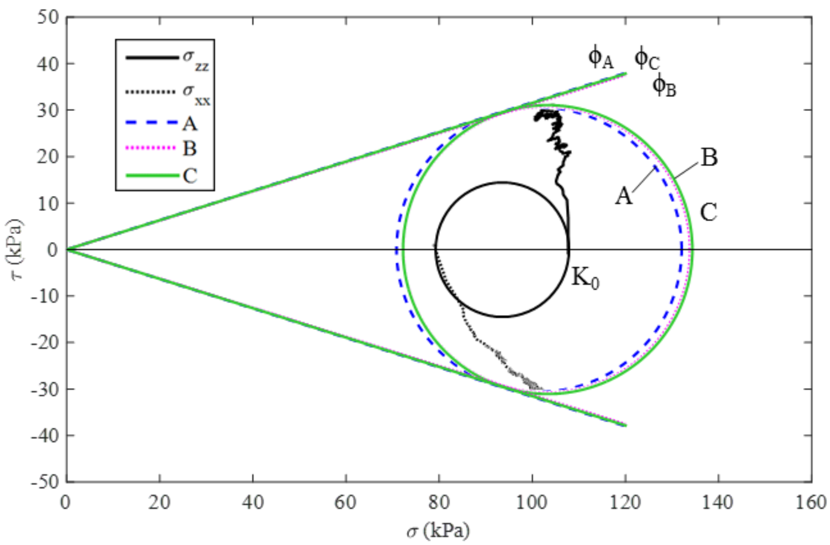

(b)

Fig. 10 Mohr's circles of stresses based on calculations within the central zone of the DEM specimen for **a** D-100 at K_0 (γ=0%), Point A (γ=3.5%), Point B (γ=9.2%), and Point C (γ=15%), and **b** L-100 at K_0 (γ=0%), Point A (γ=12.6%), Point B (γ=14.8%), and Point C (γ=15%). The strains plotted for the Mohr's circles correspond to the initial condition after consolidation (K_0) and Points A, B, and C in Fig. 9.

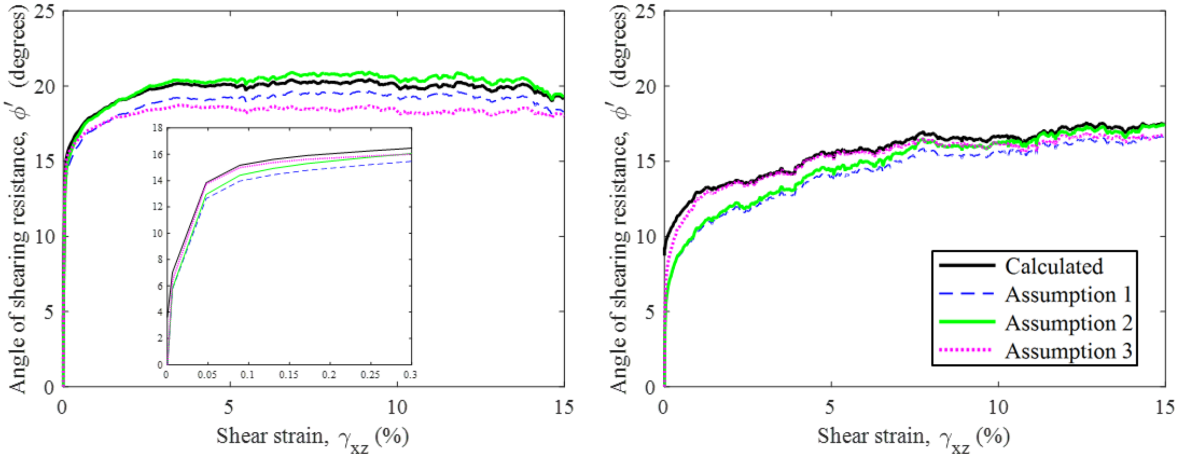

(a) **(b)**

Fig. 11 Comparison of angle of shearing resistance directly calculated from the DEM specimen and calculated using common failure assumptions for the central zone of the DEM specimen for **a** D-100, and **b** L-100.

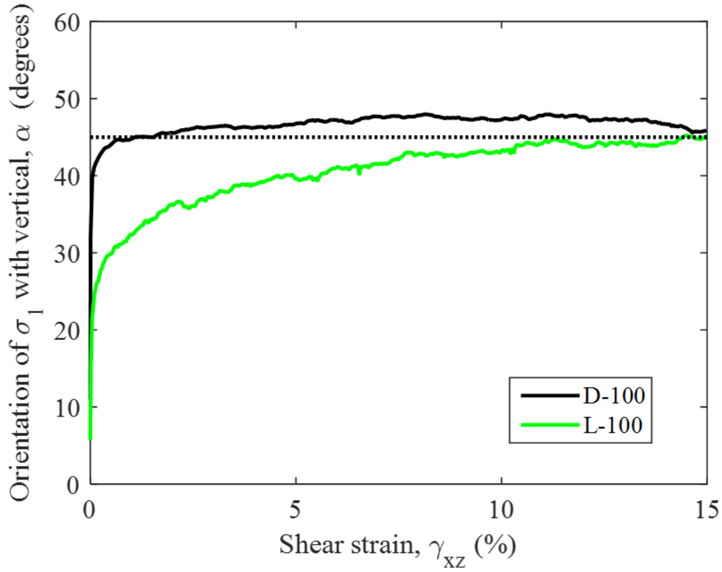

Fig. 12 Comparison of orientation of the major principal stress with vertical for the central zone of the DEM specimen for D-100 and L-100. The major principal stress orientation approaches 45° for both specimens at large strains which agrees with the angle of shearing resistance data at large shear strains.

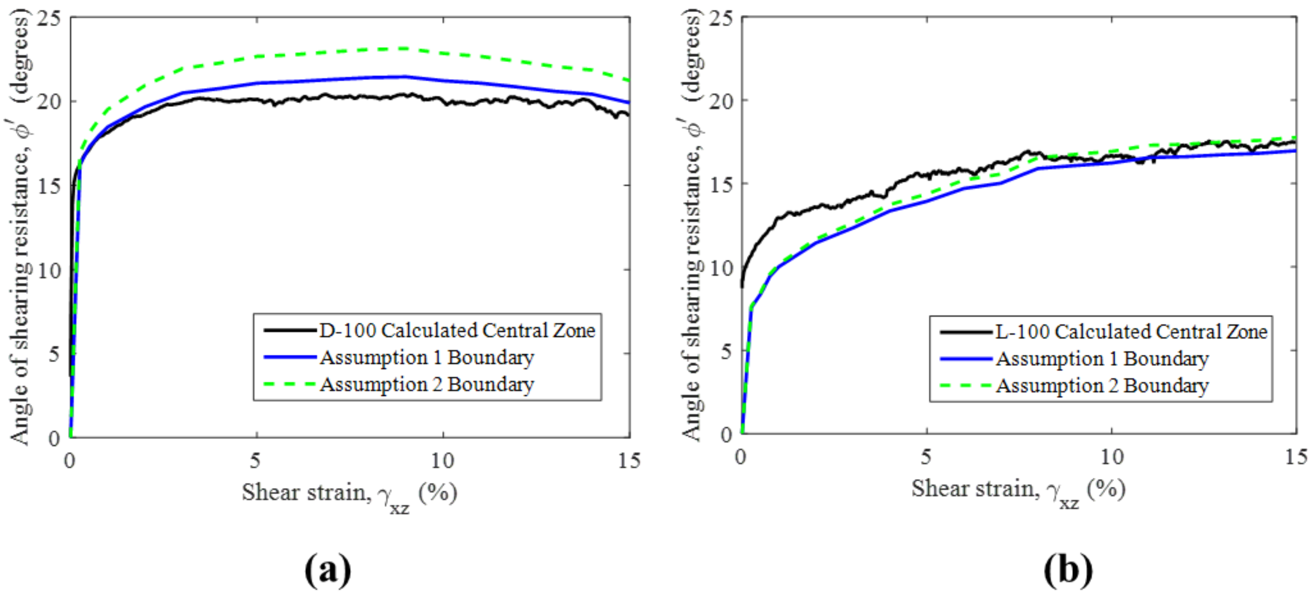

Fig. 13 Comparison of angle of shearing resistance directly calculated within central zone of DEM specimens and using boundary measurements with common failure assumptions for **a** D-100, and **b** L-100. The assumptions are calculated using effective stresses derived from measurements on the horizontally oriented DEM specimen boundary.

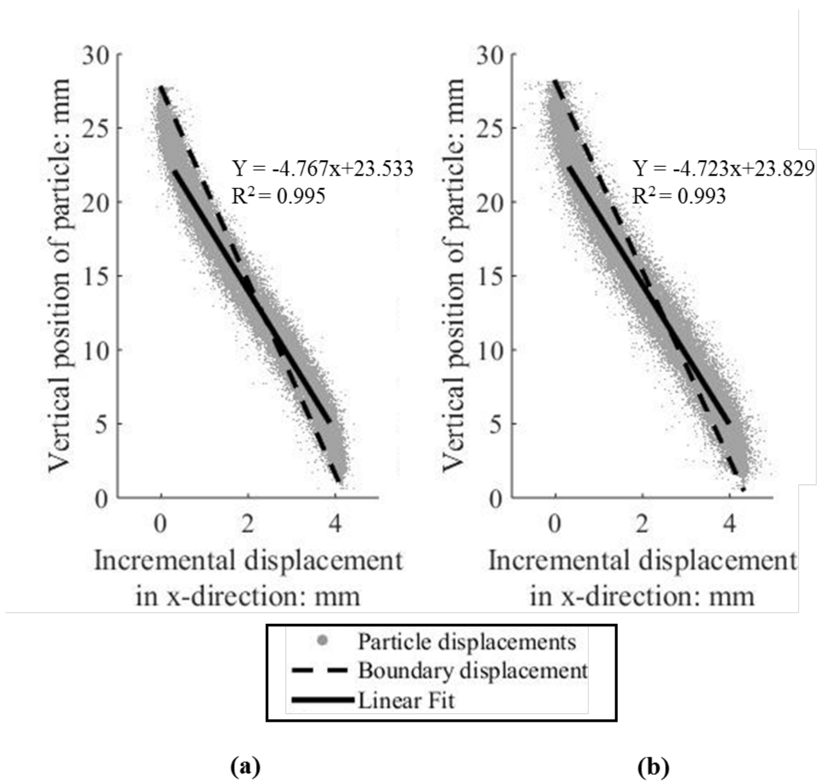

Fig. 14 Incremental particle displacements in the x-direction as a function of vertical position for a global shear strain interval of γ=0% to γ=15% within (a) D-100 and (b) L-100.

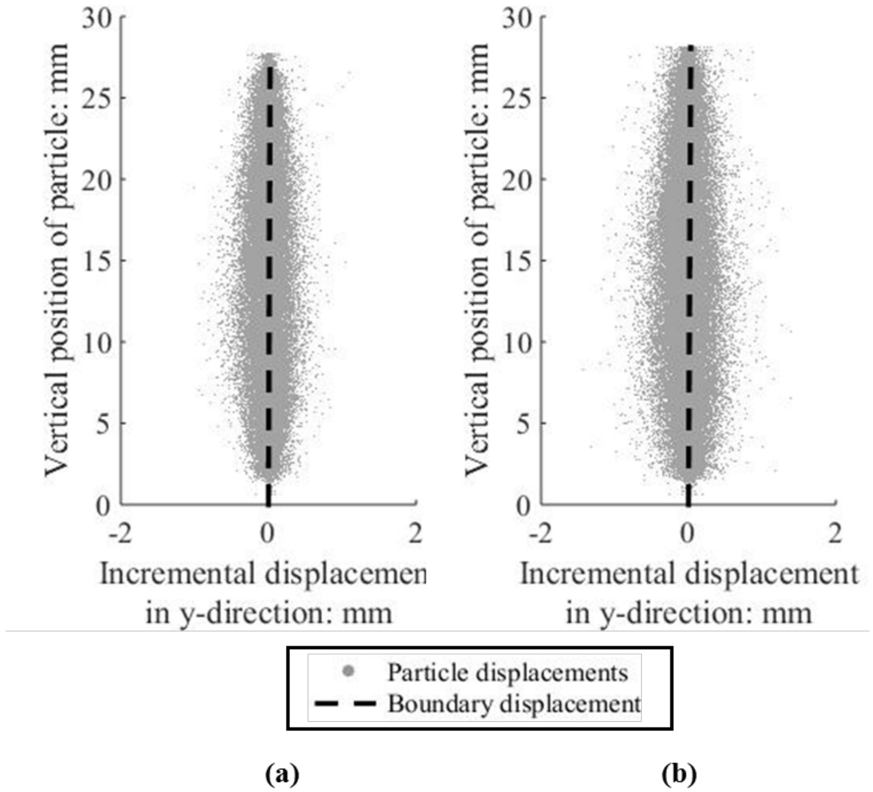

Fig. 15 Incremental particle displacements in the y-direction (out of the plane of shearing) as a function of vertical position for a global shear strain interval of γ=0% to γ=15% within (a) D-100 and (b) L-100.

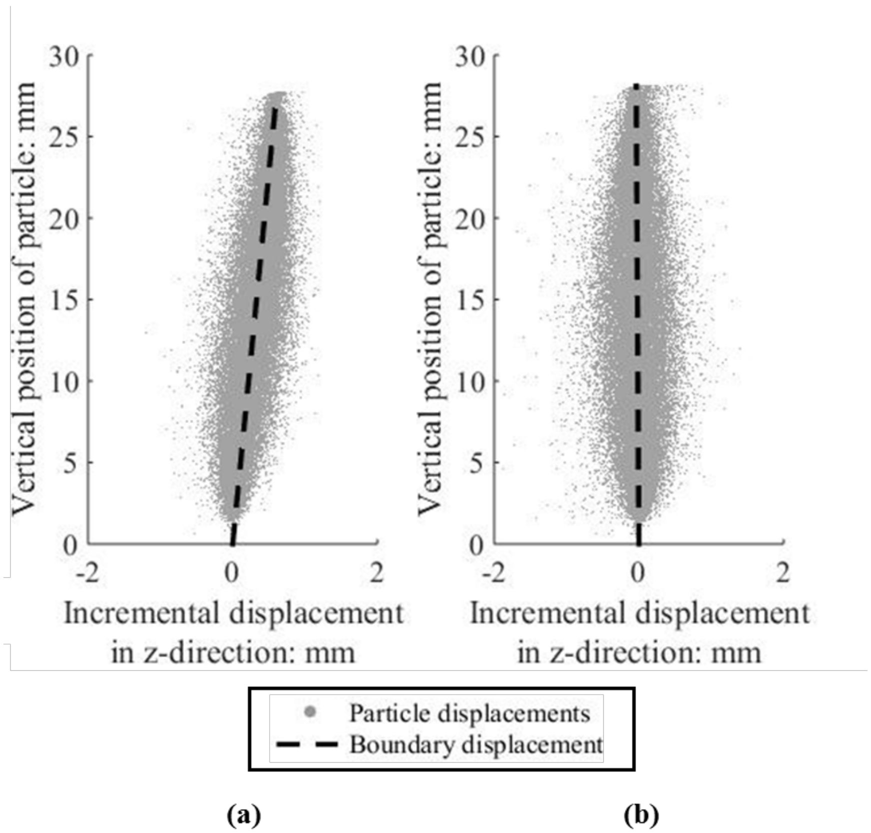

Fig. 16 Incremental particle displacements in the z-direction as a function of vertical position for a global shear strain interval of γ=0% to γ=15% within (a) D-100 and (b) L-100.

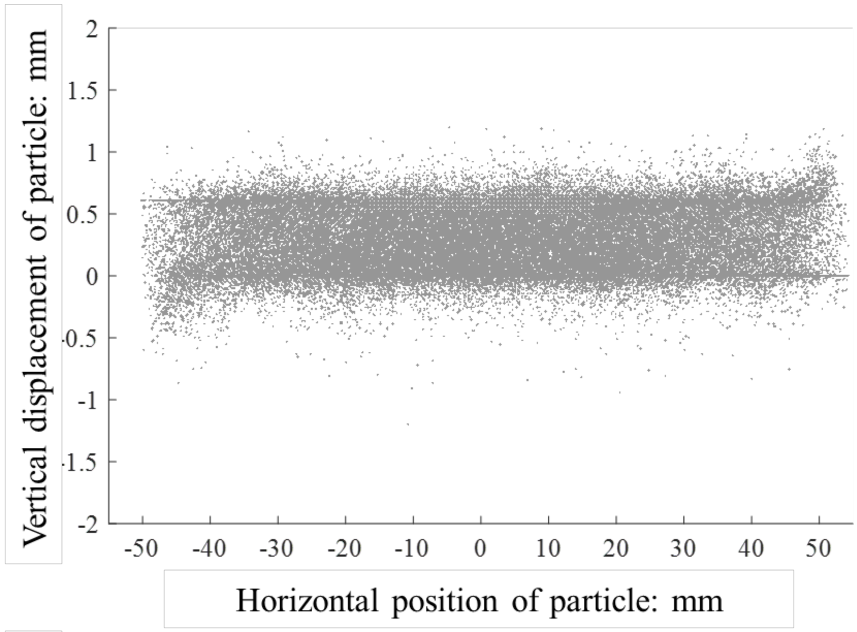

(a)

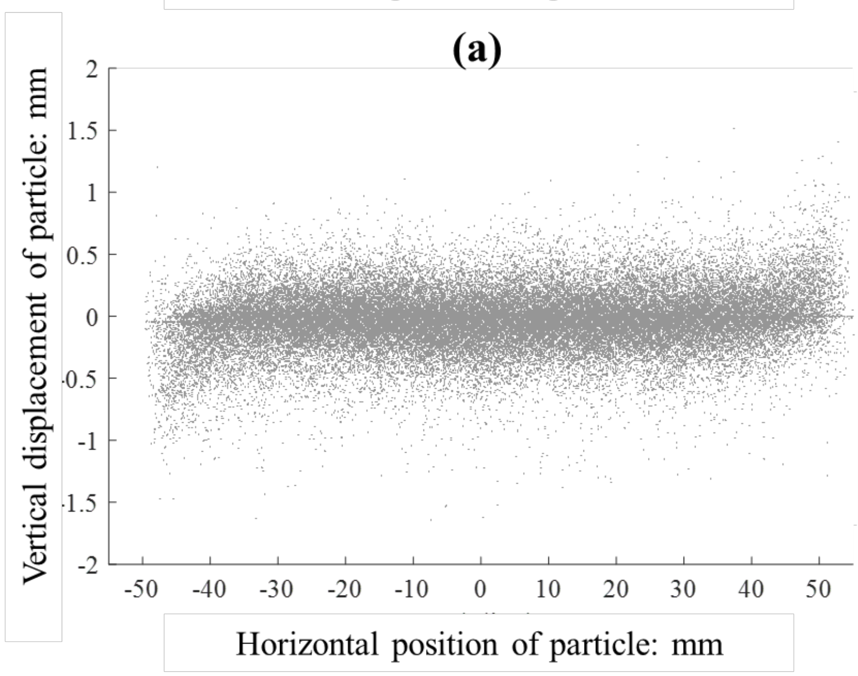

(b)

Fig. 17 Incremental particle displacements in the z-direction as a function of horizontal (x) position for a global shear strain interval of γ=0% to γ=15% within (a) D-100 and (b) L-100.

Table 1 Input parameters used in DEM simulations. The material properties were provided by the manufacturer and the friction values were determined experimentally.

Parameter	Value Used
Density, ρ (kg/m^3)	7800
Shear modulus, G (GPa)	80
Poisson's ratio, ν	0.3
Interparticle friction angle, ϕ_μ (degrees)	5.5
Interface friction angle, latex membrane (degrees)	19.8
Interface friction angle, porous stone (degrees)	23.5

Table 2 Test details including void ratio, e, and relative density, R_D, for the experimental and DEM simple shear validation tests. The initial values represent the conditions just after installation within the device at a vertical effective stress of approximately 10 kPa and the e at 100 kPa represents the conditions at the start of shearing once the specimens are loaded to a vertical effective stress of 100 kPa.

Test Designation	Initial Height (mm)	Initial e	Initial R_D (%)	e at 100 kPa
D-100-1	27.52	0.597	97.9	0.587
D-100-2	27.53	0.597	97.9	0.586
DEM D-100	27.68	0.596	100.0	0.587
L-100-1	28.52	0.654	31.5	0.633
L-100-2	28.40	0.647	38.8	0.638
DEM L-100	28.84	0.654	31.8	0.648